# Asymmetry of acceptor wave functions caused by surface-related strain and electric field in InAs

S. Loth, M. Wenderoth,* and R. G. Ulbrich
*IV. Physikalisches Institut der Universität Göttingen, Friedrich-Hund-Platz. 1, 37077 Göttingen, Germany*
(Received 22 November 2007; revised manuscript received 16 January 2008; published 24 March 2008)

The spatial distribution of the local density of states at Mn acceptors near the (110) surface of *p*-doped InAs is investigated by scanning tunneling microscopy. The shapes of the acceptor contrasts for different dopant depths under the surface are analyzed. Acceptors located within the first ten subsurface layers of the semiconductor show a lower symmetry than expected from theoretical predictions for the bulk acceptor wave function. They exhibit a (001) mirror asymmetry. The degree of asymmetry depends on the acceptor atoms' depths. The measured contrasts for acceptors buried below the tenth subsurface layer closely match the theoretically derived shape. Two effects are able to cause the observed symmetry reduction, i.e., the strain field of the surface relaxation and the tip-induced electric field. While both effects induce similar asymmetries, a comparison of their relative strengths indicates that surface-related strain is the dominant effect for Mn in InAs.

DOI: 10.1103/PhysRevB.77.115344 PACS number(s): 71.55.Eq, 73.20.−r, 72.10.Fk, 75.30.Hx

## I. INTRODUCTION

Scanning tunneling microscope (STM) studies of the local electronic contrasts induced by shallow and deep acceptors in group III–V semiconductors are subject to intense discussions.[1–8] The anisotropic contrasts of magnetic acceptors such as Mn are of particular interest because their microscopic coupling to holes and other Mn acceptors influences the macroscopic magnetic properties of the doped semiconductor.[9–11] For substitutional acceptors in zinc blende semiconductors, e.g., the group III–V compounds, one expects that the observed contrasts reflect the cubic symmetry of the host crystal's band structure (hence, $c_{2v}$).[12,13] However, shallow acceptors show up in STM topographies as triangular contrasts with the dopant atom located in the triangle's tip, clearly breaking the $c_{2v}$ symmetry.[1,2,14] Deep acceptors show an asymmetric bow-tie-like shape reminiscent of the bulk symmetry, but nevertheless, asymmetric with reference to the (001) mirror plane.[3,15] Tight-binding calculations were performed to describe the acceptor state in the bulk crystal.[3,16] Until now, the semiconductor surface was not fully included into such calculations because the necessary large slab would exceed today's computing capabilities. The probability density at the sample surface that originates from the wave function of a subsurface acceptor was extracted from the existing bulk calculation by cutting the calculated three-dimensional probability density at a certain distance from the acceptor atom and artificially adding the decay into the vacuum.[13,16] However, an acceptor in the vicinity of the surface will differ not only in electronic properties such as binding energy from a bulk acceptor but also in spatial extension of its wave function. The cleavage surface that is needed in the STM experiment to access buried dopants introduces a symmetry reduction into the system that is not included in the bulk calculations. Thus, these calculations do not completely reproduce the observed asymmetric shape, and especially not the recently reported depth dependent changes of this asymmetry.[8] In this paper, we quantitatively study the evolution of the acceptor wave function with respect to its dependence on the interaction strength with surface-related and tip-induced effects by comparative images of acceptors in different depths under the surface. The degree of (001) mirror asymmetry serves as a measure. Surface strain fields and tip-induced electric fields are discussed on the basis of band structure calculations. Both effects can explain the symmetry reduction. A comparison of their relative strengths indicates that surface-related strain is the dominant effect in this system.

## II. EXPERIMENT

The experiments are performed in a low temperature STM operating in UHV at a base pressure better than $2\times10^{-11}$ mbar. Details of the experimental setup are given in Ref. 17. The InAs samples are cleaved *in situ* at room temperature and they are transferred to the precooled microscope where they reach the equilibrium temperature of 5.6 K within less than an hour after cleavage.

To quantitatively analyze the symmetry properties of individual acceptors, we employ highly diluted samples. In fact, the symmetry analysis requires a dopant–dopant distance larger than the average Mn contrast extension of ~10 nm (see Sec. III B). On the other hand the doping has to be high enough to ensure stable STM operation at 5.6 K. A doping level of $2\times10^{17}$ cm$^{-3}$ is chosen and checked by large scale topographic STM images. The average distance of two Mn atoms in the present sample is 17 nm and is thus sufficiently large for the following analysis. Additionally, the Mn acceptor concentration establishes an impurity band with a few meV spectral widths centered at about 23 meV above the valence band edge.[18,19] The samples are conducting even at 4.2 K, which was checked by macroscopic resistance measurements.

The asymmetric contrasts discussed here are linked to the host lattice.[4,14] Knowledge of the sample's exact crystallographic orientation is crucial for the discussion. The samples are cut out of a (001) oriented wafer and the orientation of each sample piece is documented throughout the preparation process. As InAs possesses two groups of nonequivalent cleavage planes, the documented orientation of the cleavage plane is cross-checked in the STM experiment with the relative shift between empty and filled surface resonances in

 

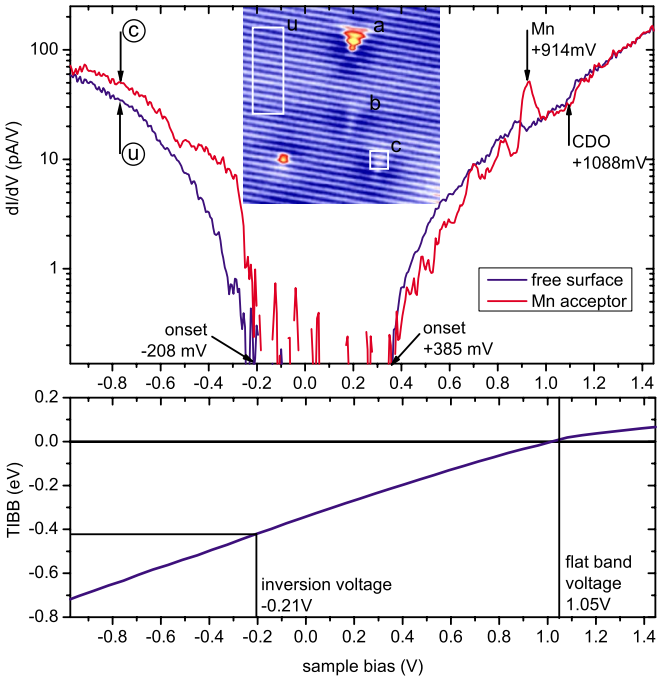


FIG. 1. (Color online) Inset: $18\times18$ nm$^2$ constant current topography of three subsurface Mn acceptors (a, b, and c) under the InAs(110) surface. The topography is recorded at +1.0 V sample bias and 100 pA tunnel current. The Mn acceptors appear as asymmetric bow-tie-like protrusions. Upper graph: local $dI/dV$ characteristics acquired in the inset topography. The blue curve (labeled with u) corresponds to the undisturbed surface and the red one (labeled with c) was recorded directly above the lower Mn acceptor (c). The topographic set point for the $I(V)$ measurement is at 2.0 V and 0.3 nA. At this set point, the Mn acceptors have no impact on the topography. Lower graph: numerically derived TIBB($V$) dependence adjusted to the presented $I(V)$ spectroscopy. The characteristic bias voltages, i.e., inversion limit and flatband bias, are marked.

spatially resolved $I(V)$ spectroscopy.[20] The measurements presented in this work are carried out on the (110) surface, i.e., the In atoms of the surface zigzag row point toward [001] (compared to the ball-and-stick model in Fig. 2).

## III. RESULTS

### A. Acceptor state identification

The first step of the analysis is the identification of the sample bias voltage at which the acceptor bound hole is imaged. The tip-induced band bending (TIBB) present at the {110} surfaces of InAs has to be considered. It causes a nontrivial relation of sample energy scale and applied sample bias.[21,22] The constant current topography in Fig. 1 presents an $18\times18$ nm$^2$ image of an atomically flat InAs(110) surface recorded at +1.0 V sample bias. The anisotropic bow-tie-like contrasts of three subsurface Mn acceptors are visible. The differential conductivity ($dI/dV$) is recorded on two spots in this region (upper graph in Fig. 1): The blue curve (denoted as $u$) is acquired in the white rectangle in the upper left corner of the topography and shows the $dI/dV$ signal of the undisturbed surface. The red spectrum (c) is recorded above the Mn contrast labeled with (c). The lower graph in Fig. 1 presents the numerically derived TIBB($V$) dependence, which has been validated with spatially resolved $I(V)$ spectroscopy in the same manner as described earlier for GaAs.[17] The actual TIBB($V$) dependence is strongly affected by parameters that vary for different tips and thus needs to be checked for each STM measurement. In order to identify the acceptor state in the $I(V)$ spectra, knowledge of the flatband bias voltage (TIBB=0 meV) is crucial. Thus, the tip work function, which determines the flatband bias, is experimentally evaluated. The TIBB($V$) is calculated using this value (4.25 eV for the presented scanning tunneling spectroscopy measurement), a typical tip geometry (15 nm tip apex radius, 90° shank slope), and an estimated vacuum gap of 8 Å. The numerical model introduced by Feenstra[22] is used. The calculated flatband bias is at 1.05 V sample bias. Delocalized charge density oscillations appear as a conductivity step in both $dI/dV$ curves at 1088 mV. This observation fixes the flatband bias to a slightly lower value than 1.09 V, which is in good agreement with the calculation. The detection of the acceptor state is expected below the flatband bias. The prominent conductivity peak at +914 mV that is solely observed above the position of the acceptor is therefore identified as the additional tunnel channel into the acceptor ground state. At positive bias, it becomes accessible when the acceptor state is lifted above the Fermi energy. Thus, the spatial distribution of this conductivity peak is associated with the direct detection of the wave function of the acceptor bound hole. The comparison of the $dI/dV$ curves above and below this peak adds further confidence to this: For bias voltages lower than +0.91 V, the acceptor state is below the Fermi energy, i.e., the acceptor is in its ionized state. No hole is bound to it and the dopant core's negative charge locally shifts the conduction and valence band states upward. The $dI/dV$ curve near the acceptor largely differs from the one recorded above the undisturbed surface. For bias voltages exceeding +0.91 V, the dopant core's negative charge is compensated by the bound hole. The surrounding area is no longer electrostatically distorted and both $dI/dV$ curves match. To conclude this section, the STM maps the probability density distribution of the Mn acceptor wave function for $>+0.91$ V bias voltage.

### B. Symmetry analysis

Further analysis is done by topographic measurements. A total of 29 acceptor contrasts is acquired in a single atomically resolved $210\times210$ nm$^2$ multibias measurement. Each line of the image is subsequently scanned with two different bias voltages before the scanner moves to the next line. Because *two* topographies are quasisimultaneously recorded, thermal drift and piezocreep between them is negligible,[23] and the absolute positions in both images match to an accuracy better than one surface lattice constant. This was verified by comparing the positions of uncharged surface point defects between both images. Figure 2 presents the zoomed images in eight different acceptor contrasts. Taking all zoomed images out of the same multibias measurement ensures that the different contrast shapes are not caused by

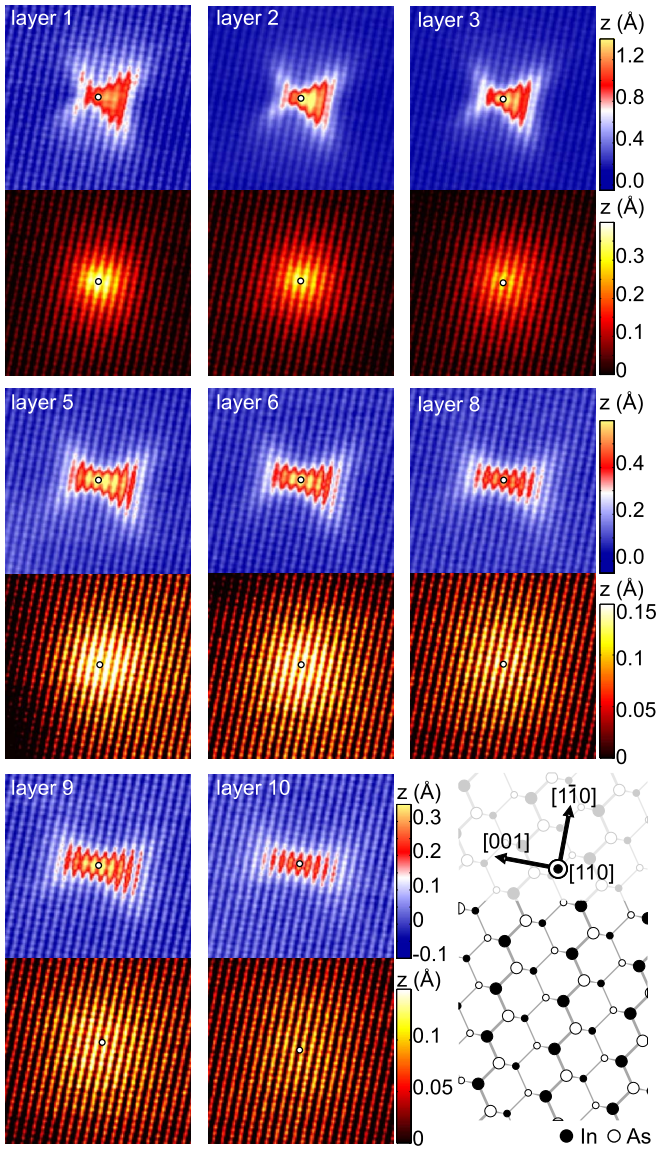


FIG. 2. (Color online) Zoomed images of $13\times13$ nm$^2$ into the multibias topography. Each image doublet shows one acceptor. The blue-red colored image is recorded at +1.0 V and the black-yellow colored images are acquired at −1.0 V. The images of one row have the same color scaling. The adjacent color bar indicates the height scale for each row in Å. The white circles show the location of the dopant atom under the surface, as determined by the center of mass and contrast maximum of the circular contrast at −1.0 V bias. The ball-and-stick model sketches the InAs lattice at the (110) surface with the orientation of the STM images. The large circles correspond to atoms of the first surface layer and the small circles are the second surface layer.

modifications of the tip's imaging properties. The two biases are chosen such that the acceptor state is imaged in one topography, while the acceptor core position can be determined in the other. The first topography is recorded at +1.0 V, i.e., directly above the acceptor state's conductivity peak. The respective zoomed images are the blue-red colored images (upper image for each acceptor). According to the $dI/dV$ curves they are an image of the acceptor bound hole's spatial distribution. The second topography is recorded at −1.0 V. At this bias, the tunnel current is dominated by the valence band states and the acceptors exhibit circular symmetric protrusions. The negative acceptor charge has a circular symmetric Coulomb potential that influences the band states.[1,2] The center of mass and maximum of this contrast resembles the projected lateral position of the acceptor core under the surface. It is indicated by white circles in Fig. 2.

The depth of each acceptor atom under the surface is determined as follows: All visible acceptors are ordered to increasing depth under the assumption that the circular protrusion in the filled state image at −1.0 V is the strongest for the acceptor nearest the surface and becomes fainter for deeper acceptors. The acceptor contrasts in Fig. 2 are ordered to increasing depth from top left to bottom right. The black-yellow colored images (lower image for each acceptor) show the evolution of the circular contrast. To pinpoint not only the monotonous depth ordering but also the precise dopant depth, additional information is used: The symmetry center of the acceptor contrasts has to follow a certain ordering with respect to the host lattice.[24,25] Mn is a substitutional acceptor on the In site. The dominant empty state resonance at +1.0 V has its corrugation maxima above the In sites of the surface zigzag row.[20] Therefore, an acceptor contrast in the first surface layer is centered directly on the corrugation maximum. If the acceptor is positioned in the second monolayer, the acceptor atom is located between the corrugation maxima. The acceptor contrasts in Fig. 2 follow the alternating on-maximum and off-maximum orderings. Recent reports suggest that acceptors located in the two monolayers that form the surface have a different appearance.[8,11] Thus, the label "layer 1" in Fig. 2 refers to the first subsurface layer. The acceptor core positions are determined for acceptors down to the tenth subsurface monolayer. The analysis shows that no acceptor was found in the fourth and seventh layer under the surface. About four to five additional depths were detected but the exact position of the respective acceptors could not be accurately determined anymore due to the vanishing feature height in the filled state image. Besides, it is worth noting that the STM could resolve acceptors that were up to 3 nm ($\triangleq$15th subsurface layer) below the sample surface. The ordered image sequence of the anisotropic acceptor contrasts (blue-red colored images in Fig. 2) shows a gradual shift from nearly triangular to rectangular shapes. The acceptor in the first subsurface layer has a pronounced triangular shape. The contrast maximum is shifted to the [00$\bar{1}$] side of the acceptor atom's location and the half-plane to the [001] side consists only of faint lobes. The acceptor in the tenth subsurface layer appears as a nearly rectangular feature centered on the dopant site. Acceptors in intermediate depths exhibit intermediate contrasts.

The degree of asymmetry with respect to the [001] direction is quantified by image analysis, as shown in Fig. 3. The topography of each acceptor is decomposed into symmetric and asymmetric parts with reference to a (001) mirror plane through the exact location of the acceptor core (blue line in the images of Fig. 3). The following conditions have to be met for this analysis.

(1) The average dopant-dopant distance has to be larger than the chosen image size. If the acceptor contrast of inter-

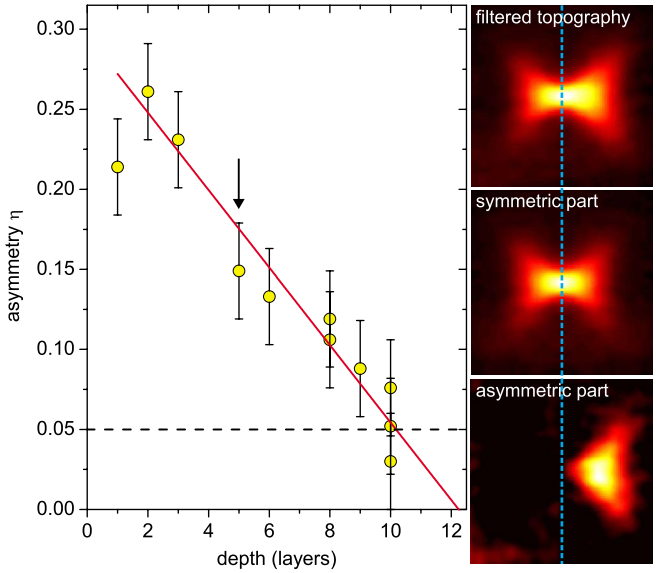


FIG. 3. (Color online) Asymmetry factor $\eta$ of the Mn acceptor contrasts plotted against dopant depth. These are the results of the symmetry analysis. If the acceptor in the first monolayer is excluded, the asymmetry decreases linearly to 0 with increasing depth. The lower limit to which the asymmetry can be detected is 0.05, which is reached for an acceptor in the tenth subsurface layer. The images at the right hand side demonstrate the symmetry analysis for an acceptor in the fifth layer (indicated by an arrow in the graph).

est was notably affected by a nearby acceptor, the symmetry analysis would return symmetry properties of the dopant arrangement rather than the symmetry properties of an individual dopant atom. Here, $13\times13$ nm$^2$ topographies are considered; hence, the average Mn-Mn distance of 17 nm (doping level of $2\times10^{17}$ cm$^{-3}$) is sufficient.

(2) The contrast asymmetry is evaluated with reference to a (001) mirror plane running through the dopant atom. Thus, the position of the Mn atom needs to be known in the topography containing the acceptor state image, i.e., at +1.0 V. However, the projected dopant position has to be determined at a different sample bias (here, at −1.0 V). Due to the employed multibias acquisition, both topographies at −1.0 V and +1.0 V precisely match and the acceptor atom positions that are determined in the −1.0 V topography are therefore also known in the +1.0 V topography.

The atomic corrugation of the surface states is suppressed in the images by fast Fourier transform filtering to minimize the background signal (upper image of Fig. 3). The symmetric part $z_s(x,y)$ is deduced from the upper image (middle image of Fig. 3). The symmetric part is subtracted from the topography, which results in an image of the asymmetric part $z_a(x,y)$ (lower image of Fig. 3). After decomposition of the filtered image, the degree of asymmetry of each acceptor contrast is given by the relative weight of symmetric and asymmetric parts. The quotient $\eta$ is a quotient of the integrals of the height information of symmetric and asymmetric images

$$\eta = \frac{\int z_a(x,y)ds}{\int z_a(x,y)ds + \int z_s(x,y)ds}.$$

It describes the ratio of the asymmetric to the symmetric components of the topography. The graph in Fig. 3 plots $\eta$ for all acceptors of Fig. 2 against the acceptor depth. The degree of asymmetry is 27% for the acceptor in the second layer. With increasing depth, the asymmetry monotonously decreases. The slope of a linear fit gives a decrease of 0.024 per monolayer depth. The detection limit for this analysis is estimated by performing the same analysis with the mirror plane $(1\bar{1}0)$. The Mn acceptor is mirror symmetric with that plane, but the value of $\eta$ varies between 0 and 0.05 for this direction because of residual noise (this limit is indicated by a dashed line in Fig. 3). The uncertainty of the symmetry analysis due to deviations in the mirror plane position determination is lower. It is $\Delta\eta=0.03$ and is plotted as an error bar. Acceptors in the tenth subsurface layer are fully symmetric within the accuracy of this analysis. According to the linear fit, the 12th layer acceptor would be completely symmetric. As a result, acceptors buried below the 10th to the 12th layer under the surface appear as rectangular contrasts that are mirror symmetric with respect to both the $(1\bar{1}0)$ plane and the (001) plane. Acceptors located within the first ten subsurface layers have a (001) mirror asymmetry. The $[00\bar{1}]$ side of the acceptor contrast is more pronounced than the [001] side.

## IV. DISCUSSION

On the basis of the local $I(V)$ spectroscopy (Fig. 1), we conclude that the asymmetric contrasts at +1.0 V are an image of the acceptor bound hole, i.e., they resemble the probability distribution of the acceptor wave function at the surface. Indeed, the observed probability density distribution of deeply buried acceptors has a nearly rectangular shape. This fits well with the theoretical expectation for a bulk acceptor as calculated, for example, by effective mass[13] or tight-binding methods.[8,16] Obviously, the spatial extension of the wave function for dopants nearer to the surface is reduced by a vertical confinement of the surface. The half-space geometry (1/2 semiconductor and 1/2 vacuum) will affect other properties, such as binding energy, as well (see, e.g., Refs. 26 and 27).

However, above all, the surface induces a symmetry reduction. The depth dependent measurements demonstrate that the probability density distribution for acceptors near the surface is deformed compared to deeply buried acceptors. Unfortunately, a *quantitative* description of surface and dopant in tight-binding calculations or *ab initio* density functional theory exceeds today's computational abilities. However, the symmetry properties of the acceptor wave function may be *qualitatively* elucidated by considerations based on the bulk band structure: The acceptor state is a hybrid of the highest valence band states. The energy window of the valence band needed to form the localized state approximately

equals the binding energy of this state.[28] The bulk Mn acceptor in InAs is 23 meV above the valence band maximum,[19] so about 10% of the Brillouin zone participates in the hybridization. The symmetry of its wave function is determined by the host crystal's band structure. If the band structure is symmetric along a certain direction, the ground state wave function will be symmetric as well. Anisotropies in the ground state wave function can only develop when the band structure exhibits this asymmetry. To good approximation, the bulk bands are cubic in this range.[29] In particular, they are symmetric with respect to the [001] direction. Effects that break this symmetry are known but usually considered to be small in the bulk, e.g., the so-called $k$-linear terms cause a splitting of less than 1 meV at the valence band edge in the bulk.[30] Figure 4(a) presents a band structure calculation for bulk InAs. Empirical pseudopotentials[31,32] were used and the spin-orbit interaction (SOI) was explicitly included.[33,34] Since the surface is not explicitly included one primitive InAs unit cell is modeled and a basis of 65 plane waves is employed.[35] The band structure is evaluated for a cut defined by a plane consisting of the [001] and [110] directions. This cut visualizes the symmetry properties of the InAs band structure that will affect the shape of the acceptor contrasts at the (110) surface relative to the [001] direction. The graph in Fig. 4 shows the energy contour lines of the highest valence band. The plotted section has an extension of about 10% of the Brillouin zone.

For the bulk system without any symmetry reducing field [Fig. 4(a)], the well-known shape ($c_{2v}$ symmetry) is reproduced. The band is symmetric with reference to the (001) mirror plane, i.e., the $[00\bar{1}]$ and [001] parts of the graph are identical. The resulting acceptor wave function will inherit this symmetry and the acceptor contrast at the surface is symmetric, as depicted in the sketch [Fig. 4(a), left]. This agrees well with the measured contrast of the "layer 10" acceptor (see Fig. 2). As a first result, an acceptor in the tenth subsurface layer has the bulk symmetry properties. The surface has no measurable impact on it. In fact, the tenth layer acceptor closely matches the previously reported theoretical predictions for the Mn acceptor wave function.[3,13] In contrast to that, our STM analysis shows that acceptors closer to the surface exhibit a strong asymmetry along [001] (refer to Figs. 2 and 3), while they remain symmetric with reference to the $[\bar{1}10]$ mirror plane. This asymmetry cannot be described with the bulk band structure only. Obviously, the cleavage surface induces a symmetry breaking that lifts the cubic symmetry with reference to the (001) mirror plane but preserves it along the perpendicular $(\bar{1}10)$ mirror plane. In the following, two effects that introduce strong changes to the band structure will be discussed: i.e., local strain fields and strong electric fields. Both are present under the STM tip at the relaxed surface.

### A. Surface effect: Strain

The atoms in the first few layers of the cleaved InAs(110) surface relax. The relaxation is usually treated in self-consistent calculations[32,36,37] and experimentally investigated by low energy electron diffraction.[38,39] In terms of strain, this relaxation decomposes into a hydrostatic component, a uniaxial component, and shear components. The uniaxial strain is along [110] for the relaxation, but neither the hydrostatic nor the uniaxial components induce symmetry breaking with respect to [001]. However, in zinc blende crystals

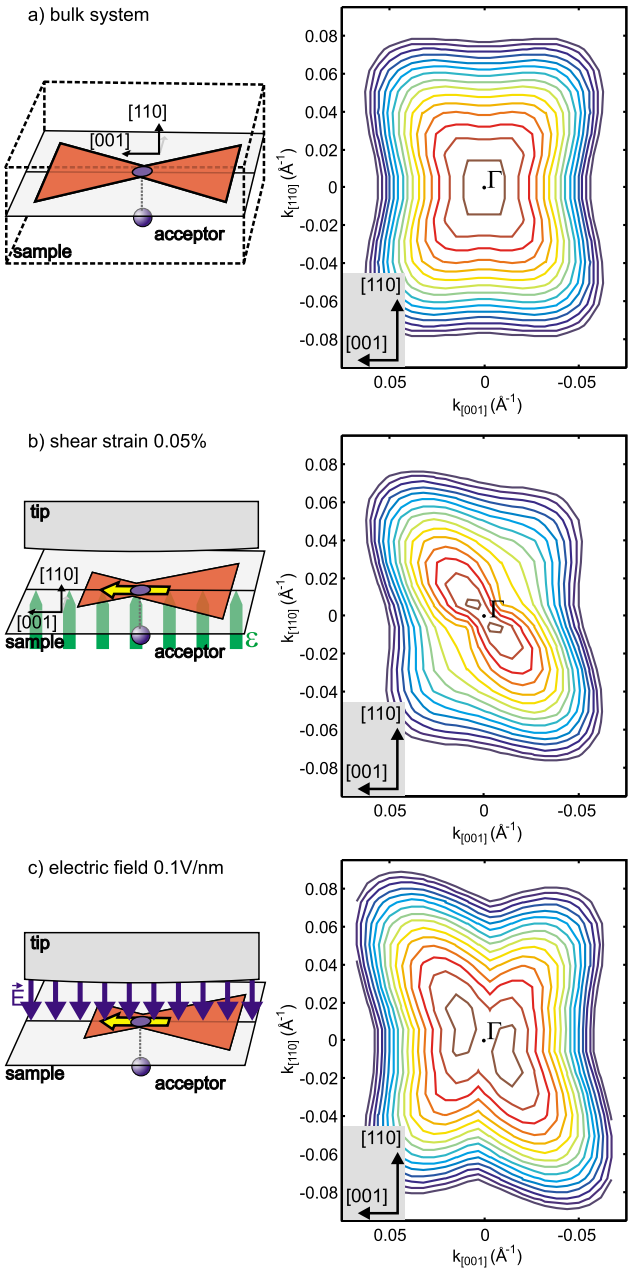


FIG. 4. (Color online) Band structure of InAs in a plane defined by [001] and [110]. The colored lines are the isoenergy lines of the uppermost valence band. The plots show about 10% of the Brillouin zone. The calculated situations are sketched to the left of each plot. (a) No additional symmetry reducing field is applied, i.e., bare InAs band structure. This results in a symmetric contrast with reference to [001]. (b) A shear strain is applied, which accounts for the strain induced by the surface relaxation. The In atoms are displaced by 0.05% of the (110) monolayer distance with respect to the As sublattice. (c) An electric field is applied along the [110] direction with a strength of 0.1 V/nm. Both (b) and (c) induce a (001) mirror asymmetry in the contrasts at the [110] surface.

uniaxial strain along the ⟨110⟩ directions results in shear components in the strain tensor.[40] They correspond to the off-diagonal components $\varepsilon_{ij}$ of the strain tensor, while the uniaxial strain is part of the diagonal components $\varepsilon_{ii}$. In recent experiments, it was shown that even small [110] uniaxial strain (that can be applied by an external vice) leads to large anisotropies in the electron propagation properties in GaAs.[41] This gives rise to the idea that shear strain of the surface relaxation induces the observed symmetry reduction along [001].

To give an estimate of whether such shear strain could lead to the observed asymmetries, its impact on the band structure is approximated within the bulk band structure calculation. It is modeled by a slight displacement of the In and As sublattices against each other. The In atom within the modeled unit cell is displaced along [110] from its equilibrium position, and under the condition of small displacements, we assume that the configuration of the unit cell is not changed. The influence of the symmetry reducing strain field on the highest valence band is shown in Fig. 4(b). The results show a prominent symmetry reduction with reference to the (001) mirror plane. Already very small distortions induce a considerable asymmetry. The graph in Fig. 4(b) shows the valence band for an In displacement of 0.05% of the [110] monolayer distance, i.e., 0.000 25 $a_0/\sqrt{2}$. The valence band becomes elongated along [111] and compressed along $[11\bar{1}]$. This asymmetry is highest for the highest valence band states. The seven inner (red and yellow) contour lines in Fig. 4(b) correspond to an energy window of about 10 meV starting at the valence band maximum. The degree of asymmetry for these states exceeds 47%. States further away from the valence band maximum are less asymmetric, but the outer (blue) contour line is still 26% more elongated along [111] than along $[11\bar{1}]$.

Recent reports of the relaxed InAs {110} surface predict that even the second subsurface layer, which is the fourth layer of InAs counted from vacuum, exhibits a [110] displacement of In and As as high as 0.5% of the monolayer distance.[42] The shear strain employed here is one order of magnitude smaller and is a reasonable choice for the residual shear of deeper layers.

This simplified model demonstrates that a small shear strain, which is present at the relaxed surface, already induces considerable asymmetry in the valence bands. An acceptor wave function in this environment will extend further along $[11\bar{1}]$ than along [111]. Thus, the probability density on the [110] surface will extend further along $[00\bar{1}]$ than it does along [001]. The resulting contrast properties are depicted in Fig. 4(b). This matches with the measurement: The asymmetric bow-tie-like contrasts are more pronounced on the $[00\bar{1}]$ side of the dopant atom. These findings are corroborated by a recent report on Mn acceptors located in the strain field of a quantum dot. The in-plane strain has a strong influence on the wave function shape of a dopant and distorts the acceptor contrast into the direction of the quantum dot.[7]

### B. Surface effect: Electric field

The second effect that is capable of producing the [001] asymmetry of the Mn contrast is the tip-induced electric field. The tip exhibits an electric field penetrating into the semiconductor. It is directed along the surface normal of the cleavage plane [110] due to the STM geometry. Typical field strengths are on the order of $10^5$–$10^6$ V/cm.[22] The STM images show that the relative weight of the acceptor wave function shifts perpendicular to this electric field. An electrostatic distortion of the wave function due to such an electric field, e.g., the Stark effect, would only produce changes that are symmetric with reference to the (001) mirror plane. An elongation or compression of the wave function along [110] would not explain the observed asymmetry. An effect is needed, which acts differently for the [001] and $[00\bar{1}]$ wave vector components. The SOI provides this kind of symmetry reduction in the band structure.[30] The above calculation is extended to implement a homogenous electric field in the [110] direction. It is introduced to the Hamiltonian via an additional SOI term in the form of the Rashba Hamiltonian.[31,34] Thus, it represents a homogenous electric field that acts solely by spin-orbit interaction. For simplicity, other effects of the external field are neglected. As illustrated by the sketch in Fig. 4(c), the electric field resembles a structure inversion asymmetry (SIA).[34] Its effect on the highest valence band is shown in the graph of Fig. 4(c) for an electric field of 0.1 V/nm. The valence band is elongated along the [111] direction and compressed along the $[11\bar{1}]$ direction. The calculated deformation of the valence band is caused by the combination of the bulk inversion asymmetry (BIA) of the zinc blende crystal and the external field induced SIA. The BIA preserves the cubic shape of the valence bands, i.e., their elongation in all ⟨111⟩ directions and compression in the ⟨100⟩ directions. The spin splitting of the bands due to SIA has a different dependence. The sign of the spin splitting due to SIA and BIA in the [111] direction is the same. Both effects add up. In the perpendicular $[11\bar{1}]$ direction, SIA and BIA have opposite signs. The sum of both effects induces the symmetry reduction over [001]. Analogous to the previously discussed strain field, this distortion is inherited by the acceptor wave function. The $[00\bar{1}]$ side of the bow-tie-like contrast will be more pronounced than the opposite side. The field strength of 0.1 eV/nm is chosen because the induced valence band distortion is similar to the distortion due to the 0.05% strain field [compare Figs. 4(b) and 4(c)]. Thus, the impact on the acceptor contrast at the [110] surface will be comparable if the tip-induced electric field is of this order of magnitude.

According to the TIBB($V$) dependence, the acceptor state is detected shortly before the flatband condition is reached. When the Mn acceptor state becomes accessible for tunneling, the TIBB is comparable to the Mn binding energy. The corresponding depletion layer involves an electric field of 36 kV/cm, i.e., 3.6 mV/nm, which is about a factor of 20 smaller than the field needed to induce enough asymmetry in the valence bands. It should be considered that the tip-induced band bending model employed here is a continuum model. In particular, the doping is assumed to be homogenous, but on the level of the STM experiment, the inherent granularity of doping becomes apparent. Thus, the electric fields present in the STM experiment will be larger than the estimates from continuum models. However, even though the

present sample is quite diluted, it is unlikely that the necessary level of 0.1 eV/nm is reached.

### C. Summary

In summary, the symmetry considerations of the band structure demonstrate that the strain field of the surface relaxation and the tip-induced electric field reduce the symmetry of the bulk band structure. Both effects act similarly on the host crystal's band structure and will thus introduce similar asymmetries in the acceptor state's wave function. A (001) mirror asymmetry is gradually developed for both cases. This is the same symmetry reduction, as observed in the experiment. The calculations indicate that the acceptor contrast should be more pronounced on the $[00\bar{1}]$ side for the [110] cleavage surface, which is supported by the measurement [compare sketches in Figs. 4(b) and 4(c) with STM topographies in Fig. 2]. Thus, both effects, i.e., strain and electric field, are capable of producing the observed (001) mirror asymmetry in the shapes of the Mn acceptors and they are *a priori* not distinguishable. Furthermore, the surface-related strain cannot be influenced in the present experiment. The tip-induced electric field is adjustable via the applied bias, but because the Mn acceptor state is only visible in topographies ranging from +0.95 to +1.1 V, the possible variation of the TIBB is only ~35 meV at the surface (see the lower graph in Fig. 1) and the concomitant variation of the electric field in the semiconductor is small. Thus, intentionally changing the strength of the electric field while monitoring the acceptor contrast asymmetry yields no significant results for this sample system.

Nevertheless, the comparison of Figs. 4(b) and 4(c) yields the estimated relative strengths of both effects and allows a differentiation: a small shear strain of 0.05% ([110] monolayer distance) originating from the surface relaxation is capable of producing a considerable mirror asymmetry with reference to (001). On the other hand, a relatively strong electric field in the [110] direction of 0.1 V/nm ($=10^6$ V/cm) is needed to introduce a similar effect solely by electric fields. Here, the Mn acceptor state is imaged near a flatband condition and the electric field is much smaller. This indicates that the surface-induced strain is the dominant effect. Additionally, the tip-induced electric field still penetrates more than 10 nm into the sample when the acceptor state is imaged. In contrast to that, the surface-induced strain rapidly decays into the crystal on a length scale of a few monolayers. Together with the rapid decrease of asymmetry with increasing depth (see Fig. 3, $\Delta\eta=0.024$/monolayer) and the observation that a Mn acceptor located in the tenth subsurface layer (2.5 nm below the surface) is almost symmetric, this lays further weight on the conclusion that the (001) mirror asymmetry is driven by a surface-induced strain field.

However, tip-induced fields of 0.1 eV/nm are easily achievable in the STM experiment. Even though the electric field is a minor effect for measurements of Mn acceptors in InAs, it should be considered in different systems, e.g., shallow acceptors in GaAs where the highly anisotropic features are imaged well within the depletion bias window when the tip-induced field is large.[17]

## V. CONCLUSION

Mn acceptors in InAs are analyzed with high resolution multibias topographic measurements. The anisotropic bow-tie-like features at subsurface acceptors are identified as an image of the probability density distribution of the acceptor ground state wave function. This is validated by local $I(V)$ spectroscopy. Simultaneous acquisition of the circular Coulomb contrast of the charged acceptor and the bow-tie-like neutral acceptor contrast allows high precision registry of the wave function image with respect to the Mn atom position. The contrast shape evolves nearly linearly from almost triangular to rectangular with increasing distance of the dopant atom from the (110) cleavage surface. Acceptors located within the first ten subsurface layers of the semiconductor have a pronounced asymmetry with reference to the (001) mirror plane that can be as high as $\eta=0.27$ (27%). The measured contrasts for acceptors buried below the tenth subsurface layer are in good agreement with theoretical predictions for the bulk acceptor's probability density distribution. In conclusion, the long-known (001) mirror asymmetry of the Mn acceptor contrasts is not only influenced by a surface-related effect, it is rather generated by it. Symmetry reduction effects at the surface, such as strain originating from the surface relaxation and electric fields induced by the STM tip are discussed as sources of the observed asymmetry. While both effects induce similar symmetry reduction, a comparison of their relative strengths indicates that surface-related strain is the dominant source in this case. These findings demonstrate that impurities in different depths under the surface give access to the evolution of wave functions in environments with varying anisotropy and/or reduced dimensionality.

## ACKNOWLEDGMENTS

We thank J. Wiebe, F. Marczinowski, and P. M. Koenraad for valuable discussions. This work was supported by DFG Grants No. SFB 602 TP A7 and No. SPP 1285, and by the German National Academic Foundation.

*wendero@ph4.physik.uni-goettingen.de

[1] J. F. Zheng, M. Salmeron, and E. R. Weber, Appl. Phys. Lett. **64**, 1836 (1994).

[2] R. de Kort, M. C. M. M. van der Wielen, A. J. A. van Roij, W. Kets, and H. van Kempen, Phys. Rev. B **63**, 125336 (2001).

[3] A. M. Yakunin, A. Yu. Silov, P. M. Koenraad, J. H. Wolter, W. Van Roy, J. De Boeck, J.-M. Tang, and M. E. Flatté, Phys. Rev. Lett. **92**, 216806 (2004).

[4] G. Mahieu, B. Grandidier, D. Deresmes, J. P. Nys, D. Stiévenard, and Ph. Ebert, Phys. Rev. Lett. **94**, 026407 (2005).

[5] D. Kitchen, A. Richardella, and A. Yazdani, J. Supercond. **18**, 23 (2005).
[6] S. Loth, M. Wenderoth, L. Winking, R. G. Ulbrich, S. Malzer, and G. H. Döhler, Phys. Rev. Lett. **96**, 066403 (2006).
[7] A. M. Yakunin, A. Y. Silov, P. M. Koenraad, J.-M. Tang, M. E. Flatté, J.-L. Primus, W. Van Roy, J. De Boeck, A. M. Monakhov, K. S. Romanov, I. E. Panaiotti, and N. S. Averkiev, Nat. Mater. **6**, 512 (2007).
[8] F. Marczinowski, J. Wiebe, J.-M. Tang, M. E. Flatté, F. Meier, M. Morgenstern, and R. Wiesendanger, Phys. Rev. Lett. **99**, 157202 (2007).
[9] S. Sanvito, G. Theurich, and N. A. Hill, J. Supercond. **15**, 85 (2002).
[10] K. Sato, P. H. Dederichs, H. Katayama-Yoshida, and J. Kudrnovský, J. Phys.: Condens. Matter **16**, S5491 (2004).
[11] D. Kitchen, A. Richardella, J.-M. Tang, M. E. Flatté, and A. Yazdani, Nature (London) **442**, 436 (2006).
[12] A. Baldereschi and N. O. Lipari, Phys. Rev. B **9**, 1525 (1974).
[13] A. M. Monakhov, K. S. Romanov, I. E. Panaiotti, and N. S. Averkiev, Solid State Commun. **140**, 422 (2006).
[14] S. Loth, M. Wenderoth, L. Winking, R. G. Ulbrich, S. Malzer, and G. H. Döhler, Jpn. J. Appl. Phys., Part 1 **45**, 2193 (2006).
[15] P. I. Arseev, N. S. Maslova, V. I. Panov, S. V. Savinov, and C. van Haesendock, JETP Lett. **77**, 172 (2003).
[16] J.-M. Tang and M. E. Flatté, Phys. Rev. B **72**, 161315(R) (2005).
[17] S. Loth, M. Wenderoth, R. G. Ulbrich, S. Malzer, and G. H. Döhler, Phys. Rev. B **76**, 235318 (2007).
[18] E. I. Georgitse, I. T. Postolaki, V. A. Smirnov, and P. G. Untila, Sov. Phys. Semicond. **23**, 469 (1989).
[19] P. T. Chiu, A. J. Blattner, S. J. May, and B. W. Wessels, Physica B (Amsterdam) **344**, 379 (2004).
[20] J. Klijn, L. Sacharow, C. Meyer, S. Blügel, M. Morgenstern, and R. Wiesendanger, Phys. Rev. B **68**, 205327 (2003).
[21] R. M. Feenstra and J. A. Stroscio, J. Vac. Sci. Technol. B **5**, 923 (1987).
[22] R. M. Feenstra, J. Vac. Sci. Technol. B **21**, 2080 (2003).
[23] J. K. Garleff, M. Wenderoth, R. G. Ulbrich, C. Sürgers, H. v. Löhneysen, and M. Rohlfing, Phys. Rev. B **76**, 125322 (2007).
[24] K. Sauthoff, *Scanninng Tunneling Spectroscopy on Single Donors and Donor Complexes near the GaAs(110)-Surface* (Cuvillier, Göttingen, 2003).
[25] A. Depuydt, C. van Haesendonck, S. V. Savinov, and V. I. Panov, Appl. Phys. A: Mater. Sci. Process. **72**, S209 (2001).
[26] M. Krčmar, W. M. Saslow, and M. B. Weimer, Phys. Rev. B **61**, 13821 (2000).
[27] K. Teichmann, M. Wenderoth, S. Loth, R. G. Ulbrich, J. K. Garleff, A. P. Wijnheijmer, and P. M. Koenraad (unpublished).
[28] A. M. Stoneham, *Theory of Defects in Solids: Electronic Structure of Defects in Insulators and Semiconductors* (Clarendon, Oxford, 1975).
[29] I. Vurgaftman, J. R. Meyer, and L. R. Ram-Mohan, J. Appl. Phys. **89**, 5815 (2001).
[30] M. Cardona, N. E. Christensen, and G. Fasol, Phys. Rev. B **38**, 1806 (1988).
[31] P. Yu and M. Cardona, *Fundamentals of Semiconductors* (Springer-Verlag, Berlin, 1996).
[32] J. R. Chelikowsky and M. L. Cohen, Phys. Rev. B **20**, 4150 (1979).
[33] W. Greiner, *Relativistic Quantum Mechanics: Wave Equations* (Springer-Verlag, Berlin, 1997).
[34] R. Winkler, *Spin-Orbit Coupling Effects in Two-Dimensional Electron and Hole Systems* (Springer-Verlag, Berlin, 2003).
[35] P. Harrison, *Quantum Wells, Wires, and Dots* (Wiley, New York, 2000).
[36] José Luiz A. Alves, J. Hebenstreit, and M. Scheffler, Phys. Rev. B **44**, 6188 (1991).
[37] A. Zunger, Phys. Rev. B **22**, 959 (1980).
[38] A. Kahn, E. So, P. Mark, C. B. Duke, and R. J. Meyer, J. Vac. Sci. Technol. **15**, 1223 (1978).
[39] S. Y. Tong, A. R. Lubinsky, B. J. Mrstik, and M. A. Van Hove, Phys. Rev. B **17**, 3303 (1978).
[40] G. L. Bir and G. E. Pikus, *Symmetry and Strain-Induced Effects in Semiconductors* (Wiley-VCH, New York, 1974).
[41] S. A. Crooker and D. L. Smith, Phys. Rev. Lett. **94**, 236601 (2005).
[42] B. Engels, P. Richard, K. Schroeder, S. Blügel, Ph. Ebert, and K. Urban, Phys. Rev. B **58**, 7799 (1998).